



Article

Quality Analysis of Weld-Line Defects in Carbon Fibre Reinforced Sheet Moulding Compounds by Automated Eddy Current Scanning

Nessa Fereshteh-Saniee ^{1,*}, Neil Reynolds ¹, Danielle Norman ¹, Connie Qian ¹ , David J. Armstrong ² , Paul Smith ³, Richard Kupke ³, Mark A. Williams ¹ and Kenneth Kendall ¹

¹ WMG, University of Warwick, Coventry CV4 7AL, UK

² Department of Physics, University of Warwick, Coventry CV4 7AL, UK

³ SURAGUS GmbH, 01109 Dresden, Germany

* Correspondence: n.fereshteh-saniece@warwick.ac.uk

Abstract: Discontinuous fibre reinforced composites enable the manufacture of integrated structural components via the complex flow process of compression moulding. However, such processes can lead to the formation of detrimental weld-lines. Here, the meso-structure of carbon fibre sheet moulding compounds (C-SMC) was analysed using conventional non-destructive techniques and automated eddy current (EC) scanning, as well as destructive methods, in an attempt to identify defects such as weld-lines in this class of materials. Compression-moulded plaques with forced weld-lines in two different configurations (adjacent and opposing flow joints) were analysed, showing up to 80% strength reduction versus a defect-free plaque. The EC-determined local fibre orientation and elucidated local microstructure matched those obtained using conventional techniques, showing a dramatic fibre tow alignment parallel to the weld-lines. It was found that failure occurred in proximity to the “non-uniformity” defect regions identified by EC analyses, demonstrating the use of robot-guided EC for successful defect detection in C-SMC structures.

Keywords: carbon fibres; discontinuous reinforcement; compression moulding; non-destructive testing; eddy current



Citation: Fereshteh-Saniee, N.; Reynolds, N.; Norman, D.; Qian, C.; Armstrong, D.J.; Smith, P.; Kupke, R.; Williams, M.A.; Kendall, K. Quality Analysis of Weld-Line Defects in Carbon Fibre Reinforced Sheet Moulding Compounds by Automated Eddy Current Scanning. *J. Manuf. Mater. Process.* **2022**, *6*, 151. <https://doi.org/10.3390/jmmp6060151>

Academic Editor: Steven Y. Liang

Received: 25 October 2022

Accepted: 17 November 2022

Published: 22 November 2022

Publisher’s Note: MDPI stays neutral with regard to jurisdictional claims in published maps and institutional affiliations.



Copyright: © 2022 by the authors. Licensee MDPI, Basel, Switzerland. This article is an open access article distributed under the terms and conditions of the Creative Commons Attribution (CC BY) license (<https://creativecommons.org/licenses/by/4.0/>).

1. Introduction

In an endeavour to reduce vehicle weight in the automotive industry, discontinuous fibre composites (DFCs) such as carbon fibre sheet moulding compounds (C-SMC) are under consideration. C-SMCs are ideal light-weighting candidates, due to their high degree of formability and consequent potential to replace highly integrated structural automotive metal components. C-SMCs offer rapid high-volume processing and excellent mass-specific performance. Owing to their discontinuous fibre reinforcement, and hence their ability to flow well, they can be used to mould complex 3D geometries in a one-shot high volume manufacturing route, which is not possible with their continuous fibre reinforced counterparts [1,2].

The mechanical properties of “forced defect free” (monolithic) DFCs in a two-dimensional format have previously been studied in the literature [3–6]. A high degree of heterogeneity has been observed in the microstructure of SMCs, with randomly oriented strands (ROS) yielding near quasi-isotropic in-plane stiffness [3,5]. However, local variations in fibre orientation and fibre volume fraction, arising because of the process-induced anisotropic microstructure, affect tensile strength due to the stress concentrations caused by discontinuities in the fibre architecture [4]. During the compression moulding process, a flow-induced meso-structure arises that can result in critical material flaws, such as resin rich pockets between the fibre tows, swirls, and trapped air (voids) [4,7]. In addition, a combination of typically complex part design, high volume fraction, and characteristic fibre length in advanced C-SMCs, promotes specific flow conditions that lead to process-induced complex

anisotropic microstructures [8], such as the formation of weld-line defects (WLDs), where two flow fronts meet.

Very limited research has been done on the formation of weld-lines in SMCs, whereas the effect of WLDs on short fibre reinforced (thermoplastic) composites has been studied to a great extent. In these cases, the effect of WLDs on the mechanical and physical properties was shown to depend on how homogeneously the two flow fronts unite [9]. Such previous studies showed that discontinuous fibres tend to reorient parallel to the WLD, decreasing the cohesion at the weld-region [10,11]. Mechanical strength can be reduced significantly after the introduction of WLDs, by up to 90% [12–14]. Lower fibre content has been reported, as well as reorientation of the fibres along the WLD, suggesting that fibres from each side are not entangled at the weld-line, as they are in the rest of the part. The direction of travel of the flow fronts also has an impact on the reduction of mechanical properties: opposing flow fronts can have a bigger detriment than flow fronts running adjacent and parallel to each other. It has, therefore, been demonstrated that the failure in short fibre reinforced thermoplastics at a WLD is governed by the nature of the mechanism that formed the interface [15].

Likewise, there has been limited research on the effect of WLDs on the performance of DFCs. LeBlanc et al. manufactured flat plaques using chopped carbon fibre tow-based composites in two configurations: “forced defect free”, and with a central WLD. It was shown that a strength reduction of between 60% and 80% occurred for the plaques with the WLD [16]. A thick compression moulded component (15 mm) was made by Martulli et al., with weld surfaces formed at different locations when the charge pattern was changed [17]. It was shown that the choice of the charge pattern configuration could play a significant role in the final part performance, particularly via the formation of weld surfaces. A recent study investigated the effect of WLD on the morphology and mechanical properties of the C-SMC [18]. It was shown that the different charge configuration resulted in strength reductions of between 48% and 88% at the WLD.

Despite the severe performance reduction caused by the WLDs, none of the above-mentioned studies applied truly non-destructive testing (NDT) methods, in an attempt to detect them; other than expensive and highly specialised techniques, such as micro-CT. At the high spatial resolutions required to characterise defects and attendant physical sample size limitations, micro-CT is considered a destructive technique and would not be applicable for in-line automated inspection at component level.

Simultaneously, accurate prediction of processing-induced microstructure using current numerical simulation methods has several limitations, such as the inability to model fibre–fibre or fibre–strand interactions, anisotropic viscosity, and simple one-way coupling [19].

Feraboli et al. reported that the use of conventional NDT methods, such as ultrasonic C-scan inspections, on DFCs proved to be difficult, due to the heterogeneity of the fibre tow distribution and orientation [7]. Typical defects that corresponded to “hot spots” in ultrasonic C-scans were voids (entrapped air at the resin-starved regions), resin rich areas, and swirls (areas of high flow, leading to fibre kinks). However, they found that failure was unlikely to occur in proximity of these hot spots, and there was no correlation between the location of the detected defects (using conventional ultrasound inspection) and the location of the final failure. Therefore, using conventional inspection methods may result in an overestimated rejection rate of parts [7].

One hitherto overlooked NDT method in the field of DFCs is eddy current (EC) testing; it has, however, been used for quality analysis and for detecting major flaws such as fibre misalignment and waviness in continuous carbon fibre reinforced polymers (CFRPs) (unidirectional, woven, and non-crimped fabrics) [14,20–26]. EC characterisation of such CFRPs relies on a high aspect ratio and the resultant anisotropic conductivity of carbon fibre tows. Due to the relatively low conductance of carbon fibre (compared to most metals), higher frequencies (in the ~MHz range) are used in EC testing of CFRPs. Due to the skin depth effect, this higher frequency will result in a reduced excitation depth within the sample, and the induced voltage, according to Faraday’s law, is proportional to rate of

change in the magnetic flux. Therefore, a higher frequency results in an increased voltage being measured by the receiver coil, giving an insight into the fibre tow orientation and the stacking configuration. A schematic of this process is depicted in Figure 1a. Heuer et al. [24] attributed the changes seen in the complex impedance signal to the three main parameters that are shown schematically in Figure 1b. First, the average electrical conductivity of the material through-thickness is a reliable measure of carbon fibre volume fraction, varying according to the amount of conductive carbon fibre (relative to the polymeric resin) in the CFRP. Moreover, the bulk conductivity of the CFRP laminate depends on the nature of the interface and connection between fibre tows, which defines the number of current paths produced by overlapping fibre bundles.

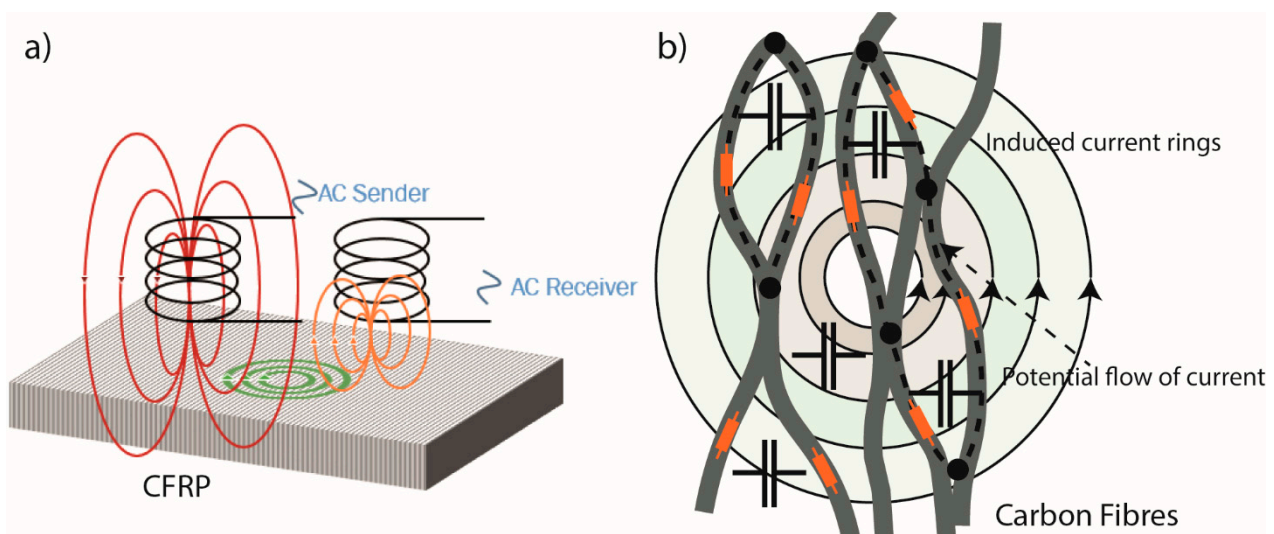


Figure 1. (a) Schematic of probe configuration for EC testing; (b) electric and dielectric behaviour of CFRP. Carbon fibre materials can be simplified as a network of resistors and capacitors, adapted from [24].

In the original work by Schulze and Heuer, a multi-frequency eddy current device was developed that was able to reveal defects underneath the surface of CFRPs, such as missing carbon fibre bundles, suspensions, fibre angle errors, and waviness [26]. Heuer et al. later used this technique to evaluate 3D parts using a radio frequency eddy current sensor [24]. It was demonstrated that both the permittivity and conductivity of the carbon fibre tows in CFRP determine the complex impedance, as measured by EC.

Whereas the EC testing of continuous carbon fibre fabrics (both dry and consolidated within a laminate) is considered an established technique, usage of the technique to examine and measure fibre orientation in chopped tow-based DFCs (C-SMC) has not previously been investigated. It is expected that localised trends in fibre orientation and fibre volume fraction within a moulded DFC will strongly influence the EC response, and particularly, a micro/meso-structural moulding defect (such as a WLD) might be detected through the changing characteristics of the EC signal. This paper investigates a new NDT approach, using automated EC scanning to examine compression moulded vinyl ester C-SMC flat plaques, with and without WLDs. This resin system was selected to meet the requirements for the C-SMC material for use in high volume manufacturing applications (automotive), and as such the material system was formulated to deliver the best balance of “mouldability”, cost, and performance.

To demonstrate the robustness of the EC scanning method, fibre volume fraction and fibre analysis results were compared between various methods, including eddy current, X-ray micro-computer tomography (micro-CT) scanning, radiograph, and process simulation. The authors propose that the novelty of this work lies in not only using EC techniques to detect WLDs in tow-based C-SMC, but also in measuring the main fibre

orientation in such materials, using a collaborative robot that can safely be placed within a manufacturing environment.

2. Materials and Methods

2.1. Materials and Manufacturing

Commercially available Polynt 24 CF60-12K SMC material (25 mm-long chopped carbon fibre-12K/vinyl ester resin fibre, weight ratio of 60%) was used in this study. All of the materials were moulded at WMG, using a flat plaque mould tool (550 × 550 mm) on a V Duo 1700 tonne press (Engel, Austria). Moulding conditions used were a tool temperature of 140 °C, clamping force of 3000 kN, closure speed of 3 mm/s, and a 180 s cure cycle.

Three different moulding charge patterns were used to create varying WLDs, as per the following (shown schematically in Figure 2):

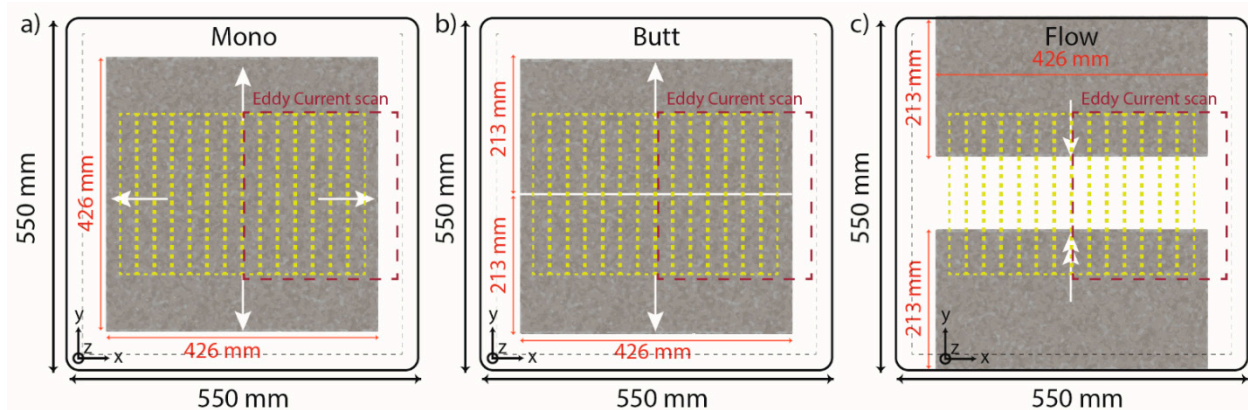


Figure 2. Charge lay-up configuration and mechanical test specimen cutting location in a full flat plaque for (a) mono, (b) butt, and (c) flow. Charge lay-up configuration and mechanical test specimen cutting location in a full flat plaque for (a) mono, (b) butt, and (c) flow.

Monolithic plaque, (Figure 2a): This was manufactured using a centrally-placed standard (continuous) 60% coverage charge, selected to eliminate the occurrence of WLDs. The charge size was 426 × 426 mm, consisting of 4 layers of SMC sheet, and it was placed in the centre of the mould.

Butt jointed plaque, (Figure 2b): Based on the standard 60% coverage charge (426 × 426 mm and 4 layers). Before moulding, a horizontal cut was made, to create a discontinuity in the charge. The split charge halves were placed immediately adjacent to each other without a visible gap (butt joint condition). This was designed to create a “low flow” joining condition across the centre of the plaque.

Flow jointed plaque, (Figure 2c): Also based on the standard 60% coverage charge (426 × 426 mm and 4 layers). Before moulding, a horizontal cut was made, to create a discontinuity in the charge. The split charge halves were then placed at opposing sides of the mould, leaving a 124 mm gap between them. This was designed to create a “high flow” joining condition across the centre of the plaque, resulting in the formation of a WLD at the meeting of linear flow fronts from each charge.

Hereafter, these three configurations are termed Mono, Butt, and Flow. In Figure 2, the yellow dashed lines show the cutting configuration for tensile specimens across all three configurations, and the pre-test EC measurement area is highlighted with a red dashed line.

2.2. NDT Tests and Microstructural Analysis

2.2.1. Robot-Based EC Measurement

A high-frequency eddy current sensor from SURAGUS GmbH, guided by a collaborative robot (Kuka-LBR-iiwa-14), was used for the EC measurements. Similar sensor technology has been used for quality assessment of carbon fibre materials [21,24,26,27]. This system permits data acquisition of the phase shift and amplitude of the EC signal in a

complex plane, as a C-scan or a time plot, by holding the EC sensor precisely at a prescribed distance during the entire scan. The scanning height is critical, as when measuring low-conductive materials such as CFRP, any distance between the test coil and the specimen (lift-off) can cause an adverse disturbance to the received complex signal, and here it was fixed at 0.1 mm.

The sensor was moved along equally spaced tracks over the surface of the moulded plaques in a raster scanning pattern. It has been shown previously that the scanning speed has no significant influence on the EC test results [28]; and in this study, a relative robot speed of 25% was used to acquire high resolution EC scans. This speed setting is related to the maximum rotational speed of the individual axes and the 25% velocity translates to a linear scan speed of 30 mm/s. Identical EddyCus sensors are already employed for in-line fibre areal weight measurements at much higher speeds, with a maximum of 300 mm/s [24,29]. A photograph of the system is shown in Figure 3. This system was integrated and supplied by Expert Tooling and Automation Ltd., Allesley, UK.



Figure 3. Photographs of the Kuka-iiwa collaborative robot equipped with the EddyCus EC sensor.

The result of the rasterised scan operation is a 2D map of the sample's electrical conductivity relative to the orientation of the sensor head during the scan. By rotating the EC sensor and performing repeated scan operations, it is possible to combine the electrical conductivity maps, to calculate variations in uniformity and main fibre orientation. Therefore, four repeated scan operations were performed for each region, and for each scan, the sensor orientation was changed from -45° to 90° , in 45° increments. Table 1 summarises the scanning parameters for the experiments, including the errors in measurements.

Table 1. Eddy current scanning parameters for the experiments.

Parameter	Value
Robot scanning speed	30 mm/s
Robot positioning accuracy (ISO 9283)	± 0.1 mm
Sensor type	SURAGUS 48
-Coil diameter	3 mm
-Shape of coil	Helical
-Coil configuration	Half-transmission
Sample rate	100 Hz
Eddy current frequency	6 MHz
Average Distance between data points	0.25 mm

In this study, all of the raw or calculated images are plotted using the magnitude of complex impedance signal defined as: $|Z| = \sqrt{(Z_{Re})^2 + (Z_{Im})^2}$; where Z_{Re} is the

real and Z_{Im} is the imaginary part of the complex impedance signal. The magnitude is independent of the phase change, and therefore no signal manipulation or phase rotation (as mentioned in [27]) was required to enhance the features of the C-SMC EC time plot images. After scanning, the imaginary and real arrays were used to plot a 2D image of the conductivity using a Python script.

Total impedance strength, also called uniformity, directly relates to the conductivity of a region, and hence is proportional to the (in-plane) carbon fibre volume fraction. Due to the inhomogeneous nature of the C-SMC, it is not practical to convert the magnitude of a complex impedance signal precisely into a fibre areal weight. As discussed, uniformity (u) (directly related to fibre areal weight) can be calculated using the magnitude (m) of the complex impedance signal measure in each sensor orientation ($n =$ different sensor directions ($-45^\circ, 0^\circ, 45^\circ, 90^\circ$)):

$$u(x, y) = \sum_{n=1}^4 (m(x, y)); \tag{1}$$

where fraction is defined as f , magnitude as m , uniformity as u , and fibre angle as fa . The ratio of material orientated towards the sensor direction (for example 0°) is defined as:

$$f_{0^\circ}(x, y) = \frac{m_{0^\circ}(x, y)}{\sum_{n=1}^4 (m_n(x, y))} \tag{2}$$

The direction of the prominent fibre angle at a particular region is given by:

$$fa(x, y) = \arctan\left(\frac{\sum_{n=1}^4 ((\cos 2 * n) \cdot f_n(x, y))}{\sum_{n=1}^4 ((\sin 2 * n) \cdot f_n(x, y))}\right) \tag{3}$$

SURAGUS GmbH uses this above approach to determine fibre areal weight measurement and to characterise anisotropy in thin films, and the formulation was hereby applied to characterise fibre angle in C-SMC [29]. The results of anisotropy measured from sheet resistance for each rotation angle of $-45^\circ, 0^\circ, 45^\circ$, and 90° are shown in the supplementary dataset.

In an attempt to understand the variations arising in the EC uniformity data, 2D radiography and micro-CT was carried out for the regions, as indicated in Figure 4. These areas showed the most complex signal attenuation, corresponding to where the material experienced the most complex flow conditions.

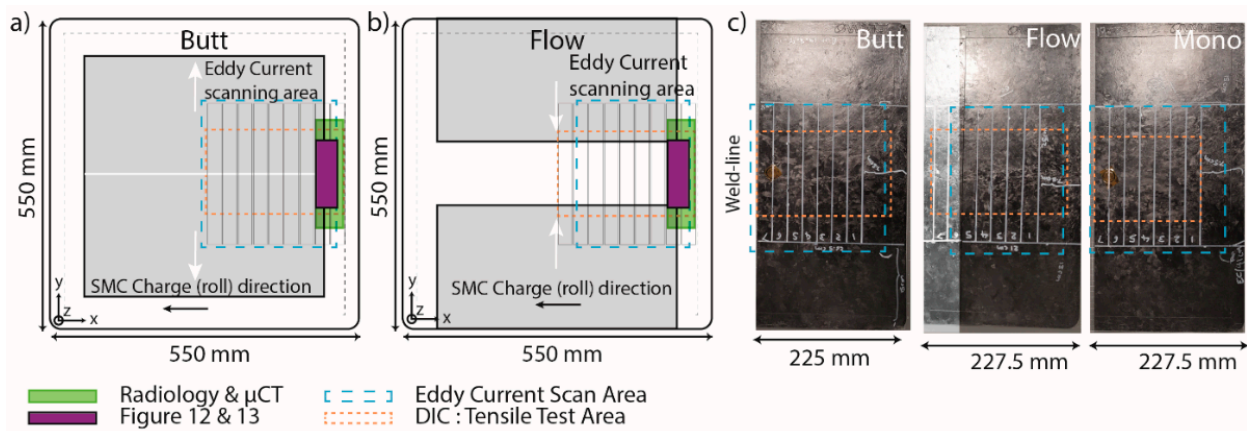


Figure 4. (a,b) DIC from tensile testing (dashed orange), eddy current (dashed blue), μ CT, and radiography (green box) area are shown for the Butt and Flow plaques. The green box highlights the location of μ CT and radiography. The purple box highlights the ROI from which all NDT and DIC images are compared; (c) DIC area is shown with a dashed orange line and the EC measurement with a dashed blue line on the actual three different plaques.

2.2.2. Micro CT and Radiography

The samples were micro-CT scanned using a Tescan Unitom XL X-ray Computed Tomography (CT) scanner at CiMAT, WMG, University of Warwick, UK. The sample is penetrated by X-rays from a cone-beam X-ray source, which are digitised by a detector into 16-bit grey value pixels, representing the X-ray absorption of the sample. Many radiograph projections are taken as the sample rotates through 360 degrees, thereby allowing reconstruction of digital 3D volumes. Alternatively, a single projection (radiograph) can be taken, where grey values are averaged through the thickness of the sample. When a sample is too large to achieve the desired scan resolution and field of view, as was the case in this work, multiple sub-scans and/or radiographs can be taken before stitching the images together. Five radiographs and three micro-CT scans of the Flow and Butt samples were conducted; X-ray parameters and sample sizes are detailed in Table 2. The focal spot size of this micro-focused X-ray source was 15 μm. Individual radiographs were stitched together using ImageJ, with contrast and brightness adjusted to maximise the grey scale range. The micro-CT scans were stitched together and reconstructed using Tescan’s proprietary Aquila reconstruction software. A first order beam hardening correction was applied during reconstruction, to normalise the grey value gradient across the width of the samples (BHC = 0.1). The reconstructed micro-CT scans were imported into VGStudio Max 2.2 (Volume Graphics GmbH, Heidelberg, Germany), a commercially available software for the analysis of CT and voxel data. The resin and fibre structures were segmented using a fixed threshold and the sample was aligned using a best-fit plane on the sample front face. VGStudio’s Fibre Analysis Module was used to determine the fibre orientation, tensor angle, and relative fibre volume fraction (the latter two were averaged through the thickness of the samples and within a 2 × 2 mm mesh). This fibre module has been demonstrated as an effective tool for analysing composite structures from micro-CT images [19].

Table 2. Tescan UnitomXL micro-CT parameters used to scan and radiograph the flow and butt flat plaques pre and post testing.

Tescan Unitom XL Parameters	Radiographs		3D Micro-CT Scans					
	Flow	Butt	50 mm Flow	50 mm Butt	25 mm Flow and Butt	50 mm Flow	50 mm Butt	25 mm Flow and Butt
Sample size (mm)	250 × 250	250 × 250	50 × 250	50 × 250	2 × (25 × 250)	50 × 250	50 × 250	2 × (25 × 250)
Field of view (mm)	297 × 262	297 × 262	49 × 49	49 × 49	54 × 54	13 × 187	13 × 192	74 × 74
Image stacking	2 × 2	2 × 2	1 × 6	1 × 6	1 × 1	1 × 5	1 × 5	1 × 1
No. sub-scans	4	4	6	6	1	5	5	1
Detector size (pixels)	2856 × 2856	2856 × 2856	2856 × 2856	2856 × 2856	2856 × 2856	1920 × 1896	1920 × 1896	2856 × 2856
Image size (pixels)	5034 × 5712	5034 × 5712	2856 × 2856	2856 × 2856	2856 × 2856	1920 × 7181	1920 × 7112	2856 × 2856
Resolution (μm)	52	52	17	18	19	26	27	26
Voltage (kV)	40	40	40	40	40	40	40	40
Power (W)	15	15	15	15	15	30	30	30
Grey range (×1000)	29–52	33–52	29–52	33–52	29–52	10–52	10–52	10–52

2.3. Process Simulation

Compression moulding process simulation was performed using 3D TIMON Composites PRESS developed by Toray Engineering D Solutions. 3D TIMON is a commercially available flow simulation software with an in-built Direct Fibre Simulation (DFS) solver, which models the movement of individual fibres in the bulk flow. The closure profile was modelled on the speed versus time data recorded by the press during the compression moulding process. The Euler method (fixed mesh) was selected in this study, and the Euler domain was meshed using an in-plane seed size of 2 mm and an out-of-plane seed size of 0.5 mm for all three cases. For the DFS analysis, a 2D random fibre architecture was generated within the volume of the initial charge using a density of 2 fibres per unit volume, and each fibre was divided into 6 linked beam elements.

2.4. Mechanical Testing with 3D DIC

Quasi-static mechanical testing was performed using an Instron test machine with a 250 kN load cell. Tensile testing was performed according to ASTM D3039/3039M [1].

Specimens were cut using a Compcut 200 composite cutting machine to a standard sample size of 250 × 25 mm and tested at 2 mm/min with a starting grip distance of 140 mm. This cutter was designed for cutting composites, hence it results in a smooth surface, as it uses a diamond abrasive wheel.

During the tensile tests, the surface strain distribution was obtained using a three-dimensional digital image correlation (3D DIC) system. DIC has been successfully used in previous studies of discontinuous C-SMC [4,30]. Here, a GOM 12M system with GOM ARAMIS software was used to capture and process stereoscopic DIC images at 1 Hz, and the system enabled corresponding data acquisition. Four static frames were recorded and analysed prior to commencing testing for each sample, to check the effectiveness of the applied stochastic pattern and to determine the noise level. The parameters of the measurements are listed in Table 3. Mean bias and precision for 3D DIC system calculated from static frames are shown in Table 4.

Table 3. DIC setup parameters.

Sensor	GOM 12 M with Titanar 100 mm Lens
Image window	4000 pixel × 3000 pixel
Measurement area	150 mm × 100 mm
Calibration plate used	CP20 90 × 72
Facet size	19 pixels (16 pixels step size)
Depth of field	39 mm
Frame rate	1 Hz

Table 4. Mean bias and precision for 3D DIC system calculated from static frames.

ϵ_x (%)		dx (mm)		dy (mm)	
Mean Bias	Mean Precision	Mean Bias	Mean Precision	Mean Bias	Mean Precision
−0.0005	0.0195	0.0034	0.0005	−0.0002	0.0006

3. Results

3.1. Effect of Different Flow Patterns on Microstructure

To better understand the effect of flow on the resultant microstructure, for the Flow and Butt samples, a 25 mm-wide tensile specimen was EC scanned and then sectioned into three pieces across the WLD region, and through-thickness micrographs were prepared using a Zeiss optical microscope. Corresponding EC real impedance maps (in-plane, top image) and optical micrographs (out-of-plane/through thickness, lower three images) are shown in Figure 5. The location of each optical micrograph section is shown on the EC maps with a coloured dotted line. It can be seen that the weld line defect extends between 5 and 10 mm, with visible cracks resulting from both the in- and out-of-plane movement of the tows.

The high-flow mechanism orients the fibres parallel to the weld line and, as a result, the reinforcement across the weld line is very poor. In this case, CF tows are no longer oriented in-plane, and the typical in-plane microstructure is locally disrupted through the thickness. The flow fronts seem to be crushed and distorted, also resulting in the formation of cracks. Similar results were shown in works by Martulli et al. [17] and Evans et al. [31]. It can be seen that the WLD region is not discrete and varies between 10 and 20 mm in width. In this case, the opposing flow front acts as a barrier that results in out-of-plane flow and alignment of the fibre tows.

Unlike the Flow plaque (which has the most of out-of-plane distortion), the micrograph of the Butt sample shows a more localised defect, and the typical SMC in-plane layered structure is restored within 10 mm of the WLD. However, the magnitude of disturbance in the EC uniformity signal seems to be much higher for this type of disturbance in the fibre architecture. It was therefore demonstrated that the action of simply splitting the charge

by mechanical cutting, and subsequently compression moulding this split charge whilst immediately adjacent, had a significant effect on the in-plane EC uniformity. The in-plane electrical conductivity remained disturbed by the original cutting of the fibre tows.

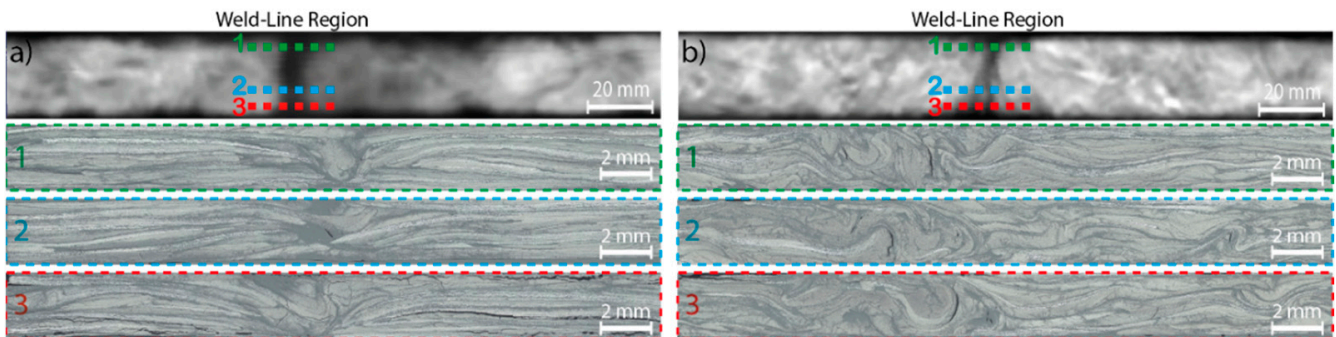


Figure 5. mm-wide in-plane EC (magnitude) image (a) Butt tensile coupon (top); (b) Flow tensile coupon (top) and three successive through-thickness (out-of-plane) optical micrographs from the same specimen region. The coloured dashed lines show the location of the cross-section depicted in the same colour dashed box.

3.2. Mechanical Properties and Comparing DIC/EC

Fourteen specimens each were tested from the Mono, Butt, and Flow plaques. All specimens with forced defects (from the Butt and Flow plaques) failed at the WLD, with no exceptions. Specimens from the Mono plaque all failed at different locations within the gauge length, as might be expected. Figure 6 shows the mean strength for each of the materials, along with the reduction in strength arising from the WLD in the Butt and Flow versus the Mono plaques. The nominal strength given by the manufacturer’s datasheet of the monolithic material at full coverage is 130 MPa. Mean tensile strengths are displayed, and the relative strength reduction is shown for the samples with induced WLDs in Figure 6.

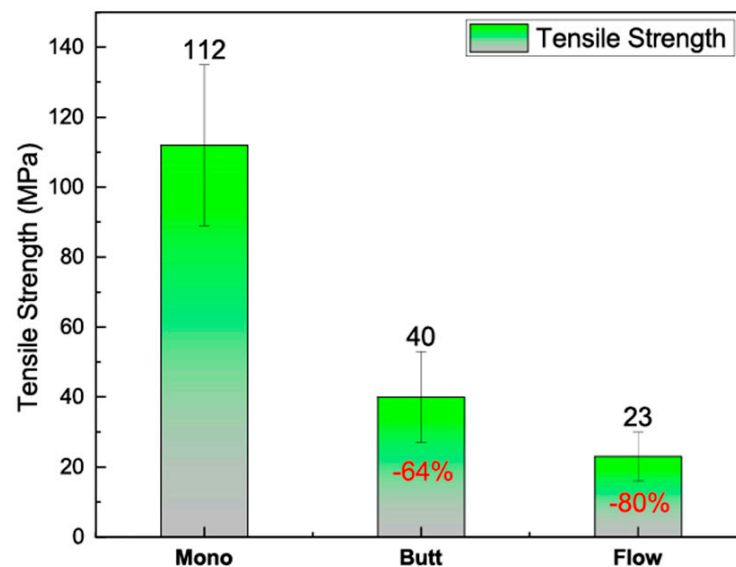


Figure 6. Tensile strength results of the three different charge patterns. Strength reductions shown for the plaques with WLDs are compared to that of the Mono plaque (WLD-free).

Figure 7 presents the EC uniformity maps for the three types of specimen (a1 (Mono); b1 (Butt); c1 (Flow)), the DIC surface strain maps obtained prior to ultimate failure during tensile testing (a2-b2-c2), and the EC principal fibre angle data (a3-b3-c3). This side-by-side comparison of the EC uniformity data/DIC data from the same regions for each material

type shows that there was some correlation between the morphology of the EC uniformity map and the local strain distributions present at the surface of the sample at failure. Local strain variations were largely associated with the non-homogeneous nature of the C-SMC, not only at the surface, but also within the underlying micro/meso-structure [30]. This is also exactly how the EC signature is governed, as the depth penetration of EC was expected to be greater than the thickness of the samples used in this study; this explains the close correlation between these EC uniformity maps and the DIC strain maps. The “hot spots” in the strain map indicate an area of the lowest modulus for the specimen, and for the Butt/Flow materials these lower modulus regions correspond exactly to the lower EC magnitude signal, as expected from resin-rich regions/locally reduced in-plane fibre orientation.

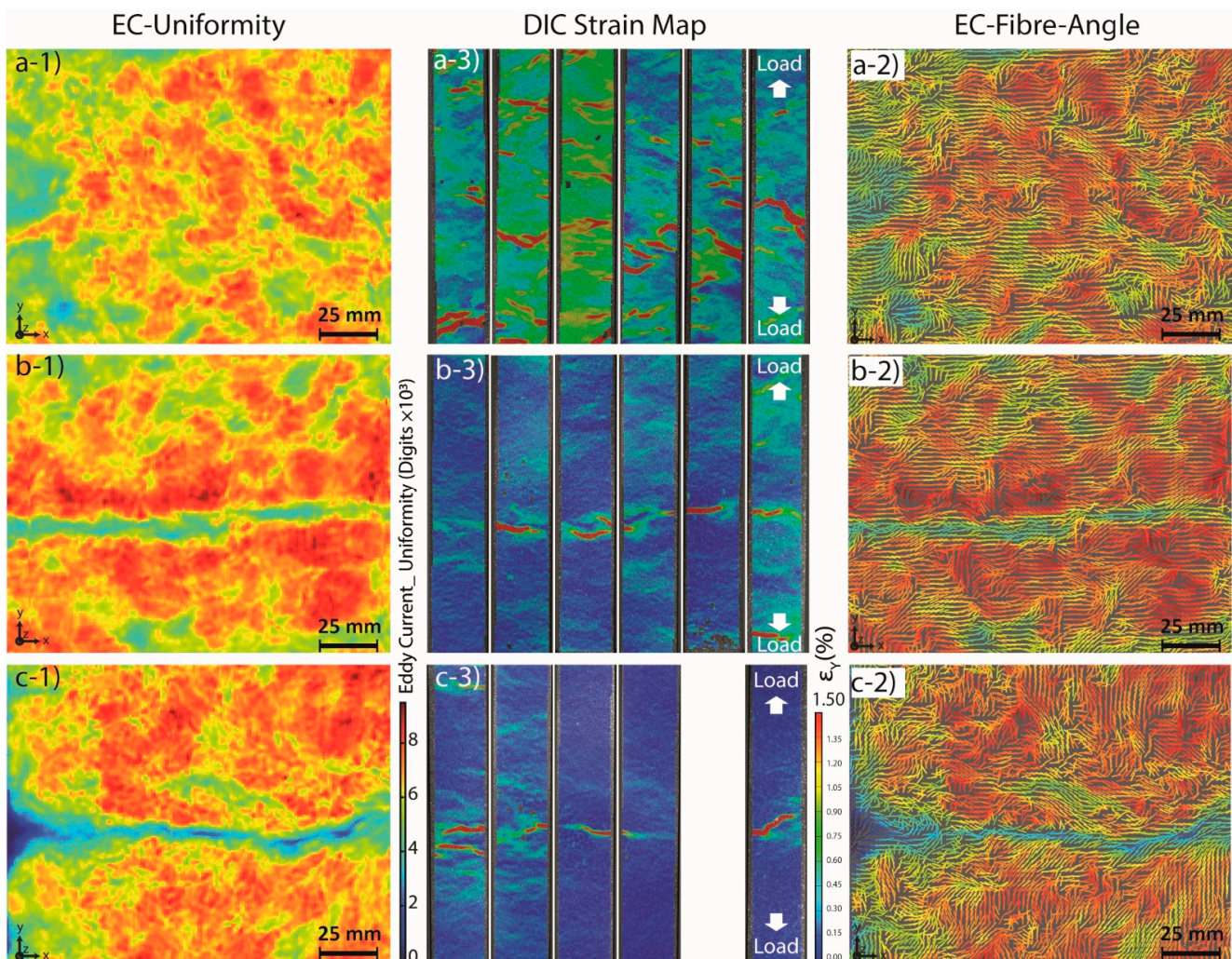


Figure 7. Comparing EC mapping (before testing) with the DIC/mechanical strength of a (a) continuous (Mono) plaque; (b) Butt (low-flow) WLD plaque, (c) Flow (high-flow) WLD plaque. (a,b,c-1) EC uniformity; (a,b,c-2) major strain (ϵ_y), fixed scale 1.5%; (a,b,c-3) main EC fibre angle with overlaid uniformity colours.

In particular, it can be seen from Figure 7(a-1–a-3) that the Mono plaque does not show the same linear discontinuity in the strain field and uniformity map as observed in the Butt and Flow plaques; there is no WLD present in the middle of the plaque, nonetheless several strain concentrations can be detected in the DIC strain maps. Considering that the original chopped tows in the SMC were of 25 mm length, large modulus variations are expected in a tensile specimen of 25 mm width. For a 25 mm fibre length SMC, the

critical RVE size is ~100 mm. The macro-scale modulus with such a small coupon size cannot be correctly captured. This gives rise to greater macroscopic heterogeneities and measurable discontinuities in the modulus [30]. The EC uniformity map from the Mono plaque confirms such a macroscopic variation in the laminate. The low intensity (blue colour) regions are ~50 mm. It is, therefore, proposed that the distribution of chips at the mesoscopic level affects the EC signal measurement at a macroscopic scale. The local fibre orientations calculated from the four-orientation EC scans of the Butt and Flow plaques (Figure 7(b-3,c-3)) indicate a high degree of transverse orientation of the fibres at the WLD (transverse to applied uni-axial load, parallel to WLD), as also reported in previous studies [15,18]. Figure 8 focuses on the results from three representative tensile specimens taken from the same location in each plaque, showing the EC local fibre angle data (superposed with the EC uniformity map) alongside DIC strain maps for each specimen at the maximum applied load before failure (σ_{\max}). The dimensions of area shown are 25 mm \times 140 mm, and the failure locations are highlighted with a dashed box. An EC map data was taken prior to cutting and testing. Note that the correlation of locations is only approximate, due to the elimination of material during tensile specimen extraction and as the DIC strain maps were obtained from deformed specimens (at σ_{\max}). The DIC ϵ_Y (axial direction) strain maps were scaled automatically (relative scaling), with the ϵ_Y (Local Max) given for each map shown (corresponding to red). Figure 8g shows the distribution of surface strains across all calculated DIC elements for each specimen, at a fixed maximum of 1.5% to facilitate comparison. More data for the rest of the specimens can be found in the supplementary data.

Again, there is close agreement between the patterns seen in the EC uniformity and the strain map for each specimen. One common feature among all ultimate failure locations is the relatively lower EC magnitude, corresponding to an increased overall resin content/lower fibre volume fraction and broken fibres. Furthermore, the calculated principal fibre angles (EC) indicate that a transverse fibre alignment (to the applied load) is dominant in the high local strain areas (DIC) and in many lower EC magnitude regions. Where these two factors combine, it is more likely that the specimen will fail, seen most clearly in the Flow example (Figure 8f(F2)). To understand if EC can provide insights about the failure location in WLD-free samples, four individual specimens are shown in Figure 9.

Taking the case of the M1, M2, and M4 specimens (Figure 9), where the failure occurred at ~45° angle in the various sections (seen clearly from the DIC strain map), it was also seen that the uniformity signal is low for this 45° section and the principal fibre orientation is also at 45°. Whilst the EC uniformity maps reveal some information about potentially weaker regions, to better predict the failure location, the local fibre orientations should also be considered. Therefore, for the defect-free (Mono) material, it is shown that EC scanning can reveal candidate locations for failure. This contrasts with what has been reported for other NDT methods (such as ultrasound C-scans), where the detected “hot spots” in scans prior to testing did not correlate with the failure location [7].

In previous studies, it was shown that strong transverse orientations parallel to the weld line can exist in high flow C-SMC parts [18]. As already discussed, this parallel orientation and a lack of intermingling leads to the observed high local surface strains and results in a highly visible disruption of EC uniformity. Furthermore, the blue resin-rich “branch-like” features seen in the EC uniformity maps for the Flow material are attributed to this local transverse orientation and poor intermingling of the CF tows. When comparing the induced WLD plaques, a clear pattern is revealed from EC and DIC, whereby the weakest part of the sample is the WLD, and this can be clearly detected by EC prior to destructive mechanical testing. The weld-line region at the centre of each specimen shows a lower EC uniformity signal and a transverse fibre orientation at the weld-line (parallel to WLD, transverse to applied stress). The combination of these two factors will certainly reduce the mechanical performance and hence the elongation to failure and strength. Table 5 summarises the mechanical properties of the three specimen types (M2, B2, and F2), as shown in Figure 8.

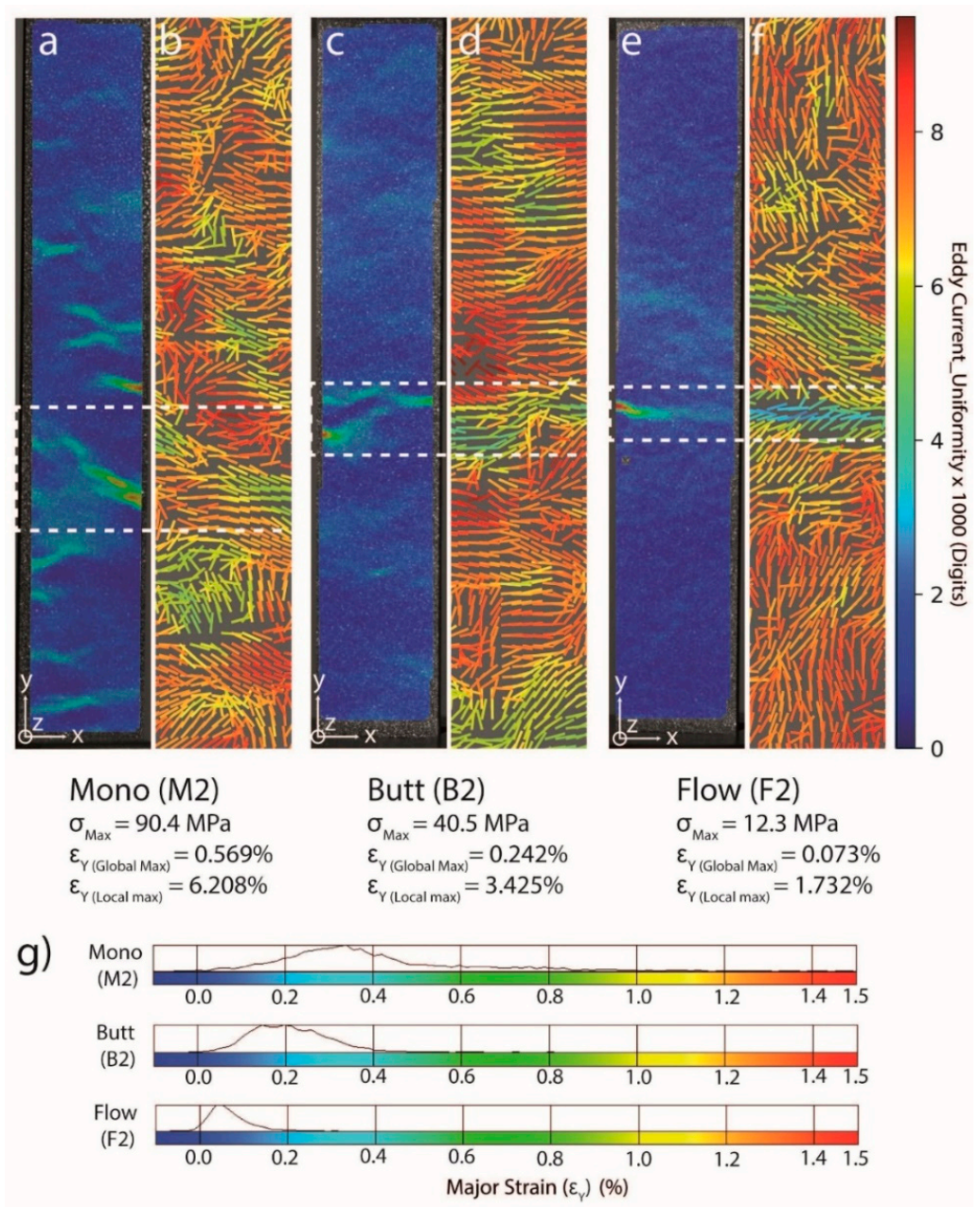


Figure 8. Comparing tensile coupons from the Mono plaque (M2, (a,b)), Butt (B2, (c,d)), Flow (F2, (e,f)). (a,c,e) DIC measurement at σ_{Max} ; (b,d,f) main EC fibre angles; (g) Comparing specimen strain distributions at σ_{Max} . (For interpretation of the references to colour in this figure legend, the reader is referred to the web version of this article). The width of each test specimen and the image is 2.5 cm.

Table 5. Mechanical properties of three specimen M2, B2, and F2 shown in Figure 8. * Please note that the modulus of the WL specimens was obtained from the “virtual” extensometer applied in the central gauge region in the DIC analyses.

Configuration	Tensile Strength (MPa)	Apparent Modulus (GPa)	Max Global ϵ_y (%)	Max Local ϵ_y (%)
Mono (M2)	90.4 \pm 0.1	16.5 \pm 0.1	0.569 \pm 0.001	6.208 \pm 0.001
Butt (B2)	40.5 \pm 0.1	* 17.2 \pm 0.1	0.242 \pm 0.001	3.425 \pm 0.001
Flow (F2)	12.3 \pm 0.1	* 16.3 \pm 0.1	0.073 \pm 0.001	1.732 \pm 0.001

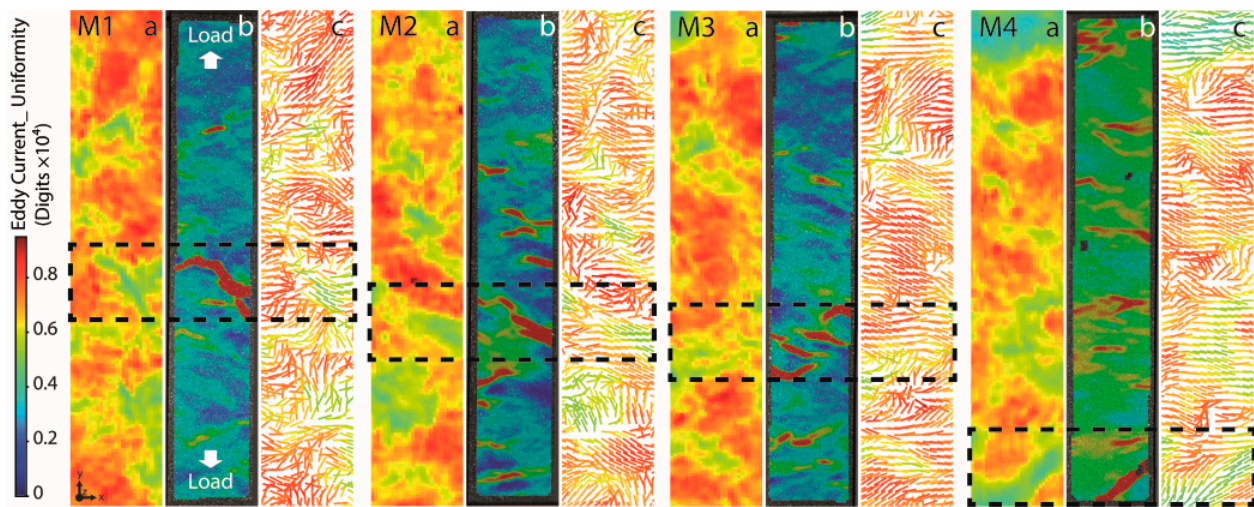


Figure 9. EC uniformity/principal fibre angle measurements along with the DIC major strain maps for tensile coupons of 2.5 cm width from the Mono sample. The maximum strain in DIC maps was set to 1.5% to enable data comparison.

It can be seen that the induced WLD did not decrease the global modulus (130 mm gauge length, calculated from DIC and across the WLD). However, the maximum tensile strength was dramatically reduced for these chosen samples for B2 and F2, by 56% and 86%, respectively. This decrease is also reflected in the changes in the DIC surface strain distributions for all specimens at maximum stress before failure (σ_{Max}), as shown in Figure 8g. For the samples with WLDs, not only is the centre of the peak of the distribution shifted to lower strains, but also the full width-half maximum of the peak has narrowed. This indicates a more discrete localised defect in the WLD specimens than for the Mono. For the Mono sample, the peak in the distribution is at a higher value of major strain than for the WLD-induced plaques (reflecting the higher σ_{Max} and also greater elongation to failure) and is also much broader. It is, therefore, harder to predict the location of failure in the Mono samples prior to failure; multiple localised strain hot-spots continue to develop across the sample during loading, up to the final failure.

3.3. Microstructure Analysis Using Micro-CT

It can be seen from Figures 10 and 11 that irregularities in the fibre tows exist, both in-plane and also in the through-the-thickness direction near the WLD for both Butt and Flow moulding configurations. Given the localised nature of the WLD irregularities, it is expected that the microstructure influences the local conductivity and reduces the EC impedance complex magnitude signal near the WLD. In Figure 10a, it can be seen that a tow of carbon fibre has an out-of-plane orientation and a crack has propagated along this tow, avoiding the nearby void in the tows. The same explanation can be used to understand the similarities seen between the high strain pattern and the low conductivity detected at the WLD. The typical mesoscopic nature of the C-SMC is no longer recognisable within the WLD region of the Flow sample. The cross-section shows that the typical defects such as macroscopic voids, swirling, and fibre kinking (and resin rich areas) are common defects at these WLDs. It appears that the failure in tow-based SMC is insensitive not only to macroscale notches [4,32], but also in smaller voids between tows near the WLD. The failure seems to run around the tow ends at the WLD and circumvents the intra tow cracks and voids, suggesting that the failure is matrix dominated. If there is a void in the weld-line, the failure crack goes through it; otherwise the voids in the bundles are unaffected and the failure is of a fibre–matrix debonding nature.

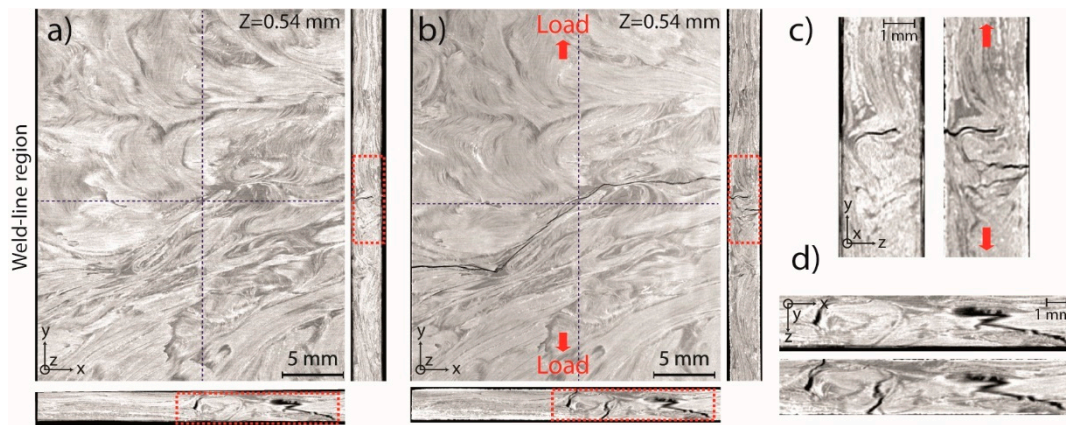


Figure 10. Flow tensile coupon micro-CT, in plane (upper) out-of-plane (lower), (a) before testing; (b) after testing; (c,d) larger sections of both scans for (c) in-plane and (d) out-of-plane, also before and after failure.

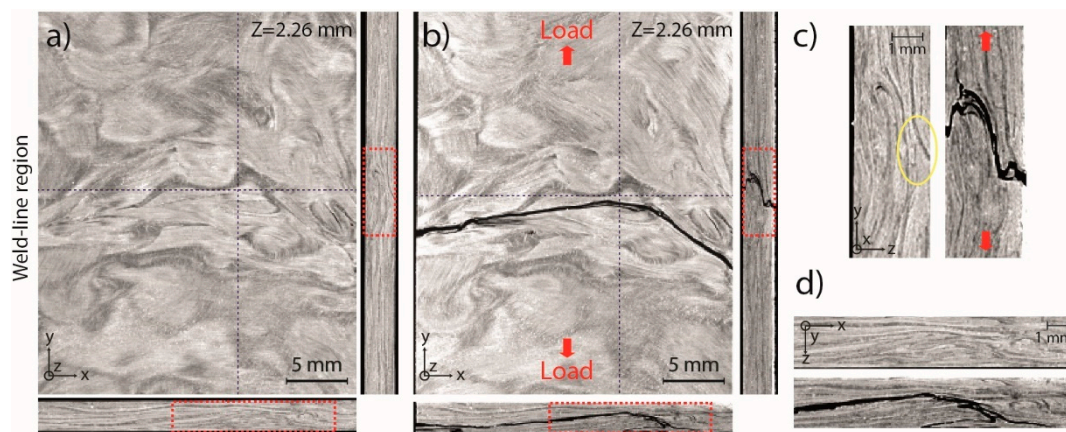


Figure 11. Butt tensile coupon micro-CT, in plane (upper) out-of-plane (lower); (a) before testing, (b) after testing; (c,d) larger sections of both scans for (c) in-plane and (d) out-of-plane, also before and after failure.

The micro-CT in-plane sections for the Flow sample (Figure 10a,b upper images) clearly show tows aligned in the direction of the WLD; in this region, it is not necessarily a horizontal line. However, the out-of-plane cross-sections (Figure 10c,d) show evidence of turbulent flow where the opposing flow fronts met. In contrast, similar out-of-plane sections for the Butt coupon (Figure 11c,d) show less out of plane movement of the fibre tows away from the WLD, as was discussed earlier for the optical micrograph. Therefore, the cross-section from the micro-CT shows similar phenomena to those seen in the optical micrograph, confirming that the out of plane flow of fibre tows are contributing to the loss of EC signal, leading to the lower intensity in the EC uniformity maps.

From the microscopy, micro-CT, and reduced EC signal (uniformity magnitude) at the WLDs, it can be concluded that the two opposing flow fronts act as an impermeable barrier, similarly to the walls of the moulding cavity, as observed by Evans et al. [31]. The out-of-plane tow distortions caused by the meeting of the opposing flow fronts are as previously shown using micro-CT [18] (characteristic bending or crushing). The discontinuities observed from the EC uniformity maps in this study at a WLD (Butt or Flow), arising from the lack of conductivity across the unbridged resin gap, confirm that there is scant intermingling happening between fibres from opposing flow fronts. In particular, in the case of the induced cut in the Butt plaque, the broken electrical circuit was not “healed” during subsequent compression moulding of the SMC. Therefore, it can be concluded that the

detrimental effects of introducing a highly localised low-flow WLD in C-SMC by placing immediately adjacent split charges remain following a high pressure co-moulding process.

In Figure 12, various features of the weld-line are examined in further detail using micro-CT. It is clear that the 2D-planar nature of the tow-based SMC was disturbed by the introduction of weld-lines. The perturbations away from an in-plane orientation cannot have been caused solely by the flow, as the orientation distribution observed by previous work for tow-based SMC showed that, for thin flat plaques, the 2D planar nature of the SMC sheets can be preserved, even in high flow conditions.

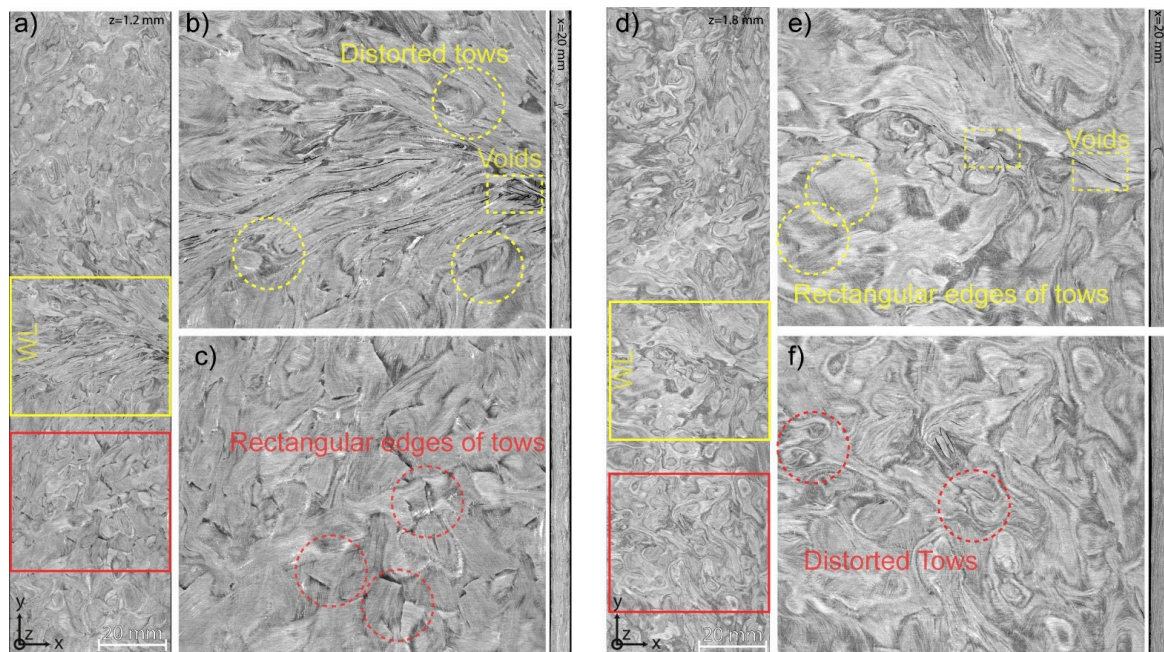


Figure 12. Micro-CT images of (a) Flow sample strip, showing two regions: (b) weld-line showing high distortion of the tow shapes, (c) away from the weld-line the tows with rectangular ends are encircled in c. The slice through is at $x = 20$ mm. ((d) Butt sample strip, showing two regions: (e) weld-line region where some tows with original rectangular shape can be seen, (f) away from the weld-line high distortion is observed. The slice through is at $x = 20$ mm, showing the planar behaviour away from the weld-line.

The micro-CT images of the strips from the Flow plaque shows that the tows are dramatically re-aligned away from the in-plane direction, transverse to the weld-line (Figure 12). None of the characteristic rectangular-shaped “chips”, as present in unprocessed C-SMC, are recognisable in this sample. Figure 12c shows that some undistorted “square” ends of cut tows can be found away from the weld-line. In contrast, the carbon fibre tows in the weld-line region have been distorted in-plane and lost all shape. It is shown below that the mechanical properties of the Flow material were lower than those of the Butt. The wrinkled/distorted tows can be seen at the flow front, explaining the significant reduction in the mechanical strength for these specimens. In the Flow sample, away from the weld-line, it appears that the material kept its mesoscopic structure. However, the high local distortion at the weld-line affected the global mechanical strength. The micro-CT images in Figure 12 were taken from the mid-section of the specimen. When examining the images in the sequence “through sample thickness”, it can be observed that higher distortion exists for the mid-plane section when compared to the outer layer in both specimens. This implies a skin–core effect resulting from a plug–flow behaviour. Darker resin rich areas and voids are seen to be more prevalent in the swirls of the distorted tows (both out-of-plane and in-plane), causing fibre waviness in all three principal axes.

In Figure 13, out-of-plane CT micrographs from the B1 Butt tensile specimen for two similar sections are shown, before and after testing for the same regions. It is clear that

the failure has run through-thickness in the resin-rich region where the fibre tows met as opposing flow fronts at the WLD. This discontinuity within in-plane fibre architecture explains the measured drop in the EC signal as the electrical circuit of the bundle tows are broken because of the non-conductive resin rich areas [24]. Minor defects such as a small round void are seen in Figure 13 and these could be as a result of air trapped between the flow fronts. Interestingly, the failure crack has propagated very close but not through the void. Similar behaviour can be seen in (b) when a crack/void in the fibre bundle is highlighted. It is therefore seen that the 2D-planar architecture of the SMC is interrupted in the WLD region of the Butt sample. The voids are more commonly seen in the resin rich areas, whilst cracks observed in the tow bundle suggest that two flow fronts do not intermingle and instead act as opposing impermeable barriers to flow. Tows become distorted as a result of this opposition. Nonetheless, away from the WLD, the typical ‘in-plane layered’ SMC structure is still visible. Comparison of the results from the process simulation with the EC uniformity scan of larger regions are presented in Figure 14.

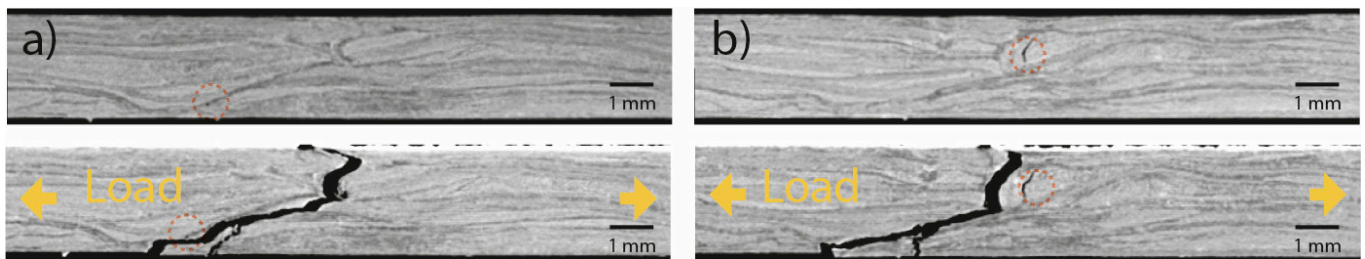


Figure 13. CT Micrograph slices of a Butt tensile specimen before and after failure. (a) A small circular void is highlighted in the resin rich area between the tows at the WLD. Even though that the crack proceeds through the resin rich area, it misses the void. (b) Another section of the same specimen, before and after testing. A larger void in the fibre tow is encircled, which remained isolated after failure, indicating that a matrix dominated failure occurred.

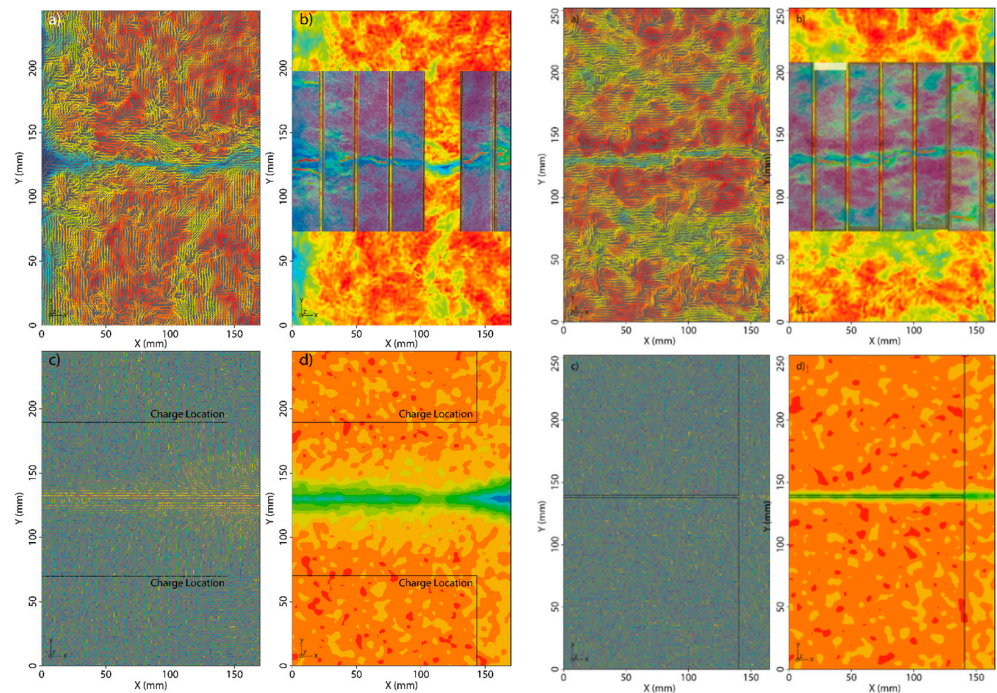


Figure 14. Comparing simulation with 3D-Timon with EC fibre angle and fibre volume fraction: (right) Flow (left) Butt.

4. Discussion

The NDT methods of advanced radiography and micro-CT, as well as DIC, were compared with EC scans for the Butt and Flow plaques for outer regions in both, where it was certain that material had flowed i.e., outside of the original charge location, as shown in Figure 4. Fibre angle analysis was performed using micro-CT, to evaluate the accuracy of the EC principal fibre angle measurements. Furthermore, the compression moulding process simulation results for these plaques are shown for the region of interest (to highlight the efficacy of EC scanning in detecting WLDs in C-SMC, which is not possible otherwise). The results for the Butt and Flow samples from the specified region of interest are compared in Figures 15 and 16.

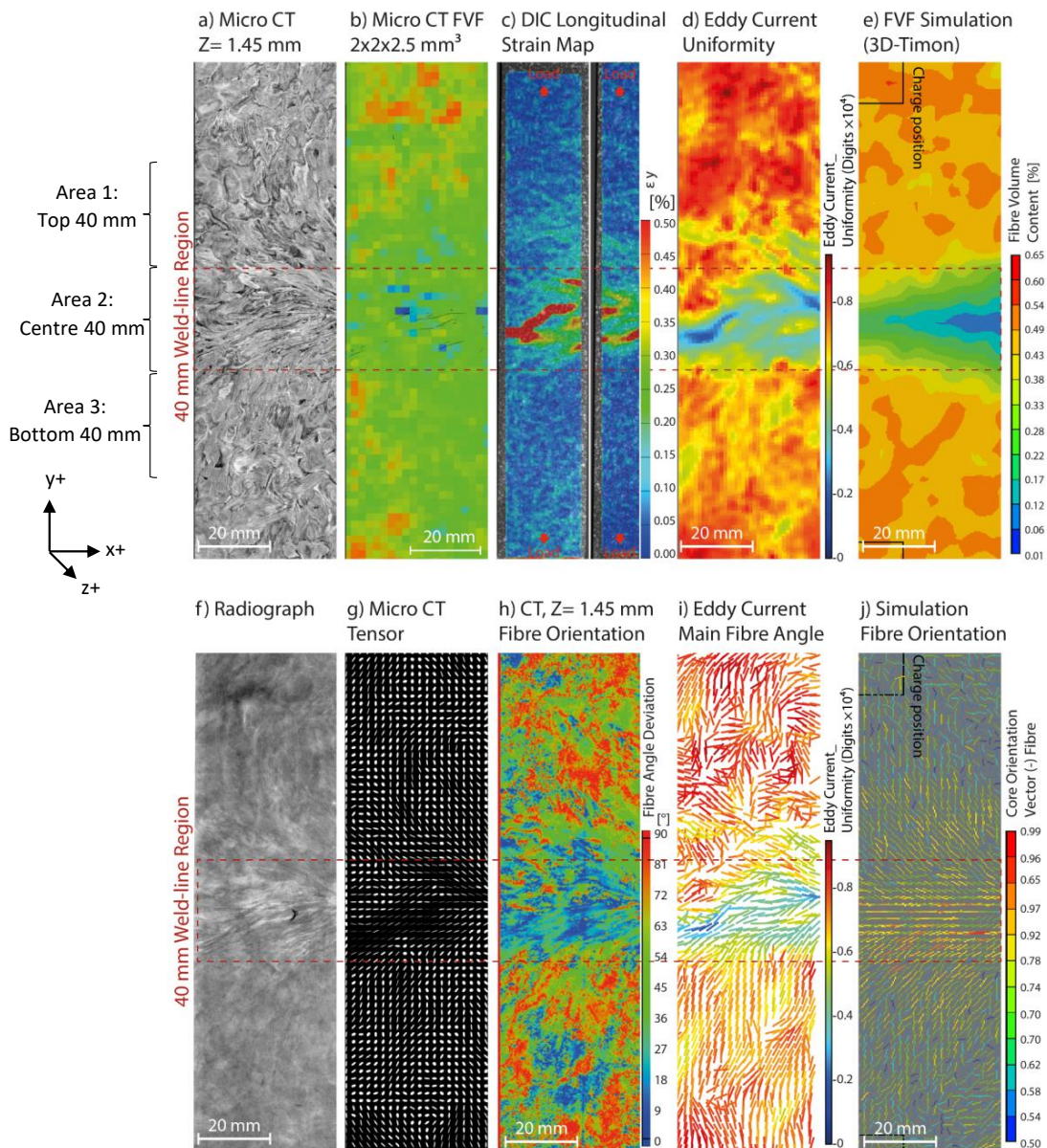


Figure 15. Comparing fibre angle and fibre volume fraction results for the Flow specimen, (a) micro CT image (at $z = 1.48$ mm), (b) micro-CT relative FVF, (c) DIC longitudinal strain map of two adjacent tensile coupons (max strain at 1%), (d) eddy current uniformity (fibre areal weight), (e) simulated fibre areal weight, (f) radiograph, (g) fibre tensors (micro-CT), (h) micro-CT fibre orientation (at $z = 1.48$ mm), (i) eddy current principal fibre angle, and (j) simulated fibre orientation. The WLD areas are highlighted with a red dashed box. Dimensions of area shown are $39 \text{ mm} \times 135 \text{ mm}$.

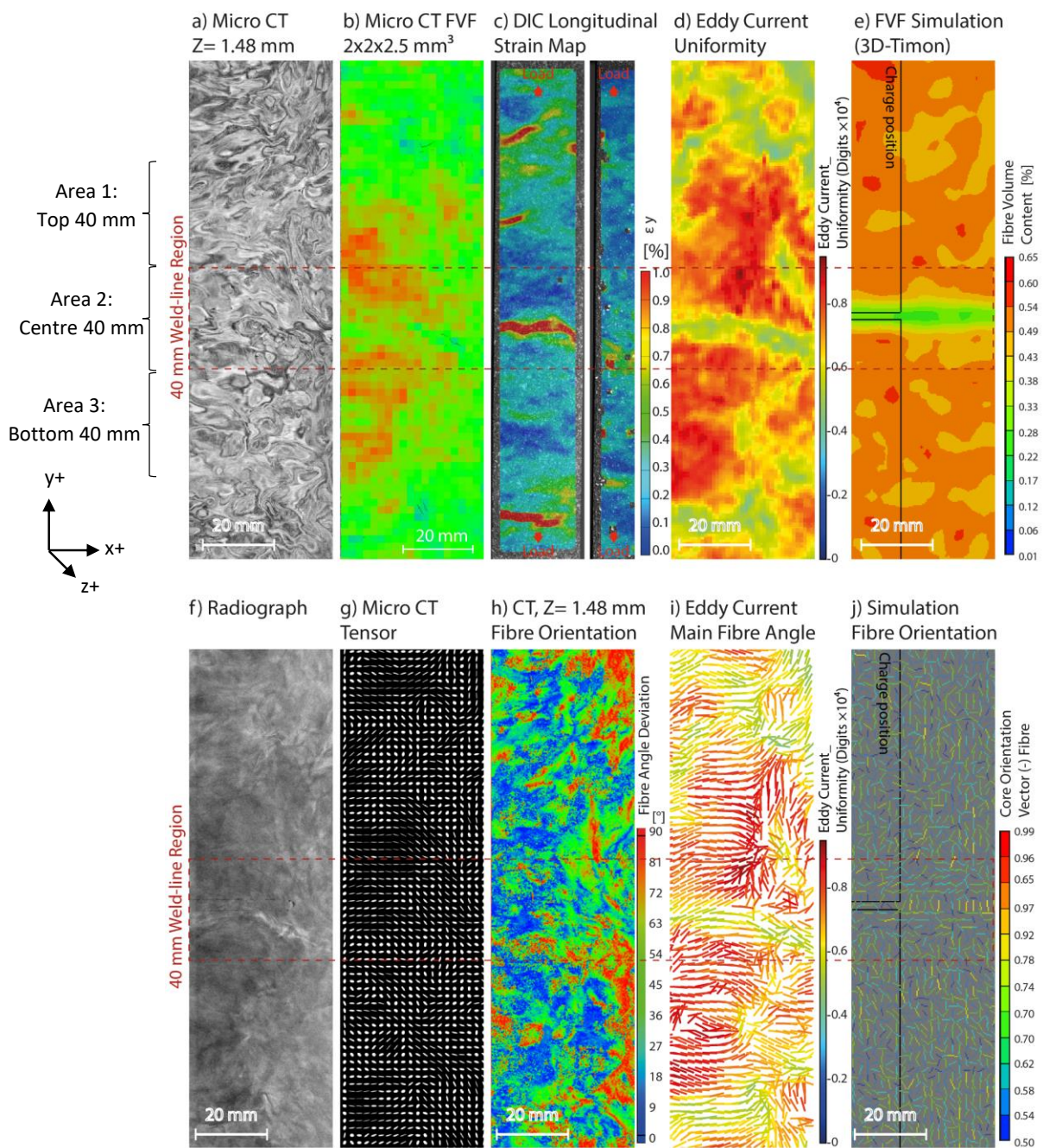


Figure 16. Comparing the fibre angle and fibre volume fraction results for the Butt specimen, (a) micro CT image (at $z = 1.45$ mm), (b) micro-CT relative FVF, (c) DIC longitudinal strain map of two adjacent tensile coupons (max strain at 0.5%), (d) eddy current uniformity (fibre areal weight), (e) simulated fibre areal weight, (f) radiograph, (g) fibre tensors (micro-CT), (h) micro-CT fibre orientation (at $z = 1.45$ mm), (i) eddy current principal fibre angle, and (j) simulated fibre orientation. The WLD area is highlighted with a red dashed box. Dimensions of area shown are $39 \text{ mm} \times 135 \text{ mm}$.

As before, there is some correlation between the DIC strain measurement (c) and EC uniformity maps (d), as the microstructure and local fibre volume fraction (FVF) directly influenced the stress–strain distribution in C-SMC. The EC sensor picks up the superposition of magnetic field contributions through the entire thickness, coming from the flow of current within the C-SMC. Each chopped bundle/layer will contribute differently to the overall magnetic field, and thus the impedance measured by the EC coils. Cheng et al. predicted, using finite element analysis, that the current density is at a local maximum when

fibre tows cross [23]. The WLDs are seen to provide the opposite effect to that witnessed at interfaces between cross-ply, due to the demonstrated lack of intermingling where the two flow fronts meet. Therefore, a local minimum of current density can be expected for all layers of the C-SMC. A measurable difference in the complex contribution is shown when looking at the total impedance strength scans from the combined four-direction EC scans (d). This is further emphasised when looking at the microstructure in the micro-CT data (a). To replicate the fibre angle measured by EC using micro-CT, a volume of $2 \times 2 \times 2.5$ mm was chosen to calculate the fibre tensors shown in (g) and also to measure the relative FVF through the thickness (b).

However, this is not the only factor that leads to such a reduction in the ultimate strength. Away from the weld-line (also in “forced defect-free” materials), a complex EC uniformity map was obtained that correlates with the radiographs (f) of the same part showing a lower intensity. It was shown earlier, in Figures 7 and 9, that the EC uniformity map in “forced defect free” material has an associated strain distribution map with corresponding minima and maxima throughout the sample, showing that the observed variation in local modulus is “material inherent” to DFC. It was previously shown that these materials are virtually notch insensitive at the macro-scale [4,32].

It can be seen from Figures 15 and 16 that the weld-line region shows a lower in-plane/FVF carbon content (lower uniformity EC signal), thus agreeing with the simulation results (e), micro-CT FVF (b) and the radiographs (f). However, the morphology of variations in microstructure is not in agreement when comparing EC uniformity (d) and predicted FVF from simulation (e) in Figure 12. It demonstrates that the simulation cannot replicate the complex flow behaviour at the meeting flow fronts and hence cannot predict the resultant microstructure.

In Figure 15, in the region adjacent to the WLD, a 45° principal fibre angle is predicted by the simulation (j) and this is in agreement with both micro-CT tensor (g), fibre orientation data (h) and EC principal fibre angle (i). However, the process simulation predicted higher level of fibre alignment along the WLD, due to the inappropriate constraints imposed to the fibres at the flow front. The imprint of the WLD can be seen in radiographs (Figure 15f) and the micro-CT images (Figure 15a). These correlate with the DIC strain maps (Figure 15c) highlighting that the failure occurred at the weld-line where the EC uniformity showed the weakest signal (prior to testing). Some correlation between the relative FVF measured by micro-CT (b) and the EC uniformity signal (d) can be seen in Figure 16, indicating unexpected WLD formations (at 45°) in this region near the edge of the mould. Process simulation fails to replicate such process-induced features possibly due to the flow front effects caused by the DFS model. The fibre angle measurements observed in Figure 13 again reveal that the fibres are oriented parallel to the weld plane (Figure 16g,i). Therefore, using the EC principal fibre angle data and EC uniformity map, it is proposed that failure location could readily be predicted.

Tables 6 and 7 show the mean orientation tensors measured using Micro-CT, Simulation and Eddy Current for Flow and Butt specimen of scanned areas marked as 1, 2 and 3. The area that these tensors were measured and the coordinate system are shown in Figures 15 and 16 for Flow and Butt samples respectively. The red dashed area corresponds to Area 2 (weld-line region) in both specimens.

The measured out-of-plane orientation is higher in area 2 of both specimens according to Micro-CT and simulation results, and this is in agreement with results reported in [18]. This outcome is connected to the tows’ high out-of-plane distortion seen in the Micro-CT slices shown in Figures 10, 11 and 13.

The values of both A11 and A22 for both specimens are close to 0.5 in the two scans (Areas 1 and 3 in Figures 15 and 16) below the weld lines, this is more characteristic of a 2D uniform random tow orientation. The main difference can be seen in the A11 values of the scan results of Area 2. A11 of the Flow samples is higher than that of the Butt specimen at the weld-line area that demonstrate a stronger dominating orientation parallel to the weld-line when compared with the Butt sample, as would be predicted given the considerable

in-mould flow. Particularly, Table 7 shows A11 components of 0.64 for Flow and 0.54 for Butt, which are comparable to the measured values for the orientated specimens in [11].

Table 6. Mean orientation tensor measured for the Flow specimen of scanned area, marked as 1, 2, and 3, using Micro-CT, simulation, and eddy current. The failure location is highlighted in red.

Flow Joint	Micro-CT	Simulation	EC (2D Measurement)
Area 1: 40 mm above the WL	$\begin{pmatrix} 0.55 & 0 & 0 \\ \text{sym.} & 0.44 & 0 \\ \text{sym.} & \text{sym.} & 0.01 \end{pmatrix}$	$\begin{pmatrix} 0.46 & -0.09 & 0 \\ \text{sym.} & 0.54 & 0 \\ \text{sym.} & \text{sym.} & 0 \end{pmatrix}$	$\begin{bmatrix} 0.59 & . \\ . & 0.41 \end{bmatrix}$
Area 2: ±20 mm around the WL	$\begin{pmatrix} 0.64 & 0.03 & 0 \\ \text{sym.} & 0.33 & 0 \\ \text{sym.} & \text{sym.} & 0.03 \end{pmatrix}$	$\begin{pmatrix} 0.61 & -0.03 & 0 \\ \text{sym.} & 0.39 & 0 \\ \text{sym.} & \text{sym.} & 0 \end{pmatrix}$	$\begin{bmatrix} 0.67 & . \\ . & 0.33 \end{bmatrix}$
Area 3: 40 mm below the WL	$\begin{pmatrix} 0.52 & 0.03 & 0 \\ \text{sym.} & 0.47 & 0 \\ \text{sym.} & \text{sym.} & 0.01 \end{pmatrix}$	$\begin{pmatrix} 0.44 & 0.08 & 0 \\ \text{sym.} & 0.56 & 0 \\ \text{sym.} & \text{sym.} & 0 \end{pmatrix}$	$\begin{bmatrix} 0.38 & . \\ . & 0.61 \end{bmatrix}$

Table 7. Mean orientation tensor measured for the Butt specimen of scanned area marked as 1, 2, and 3 using Micro-CT, simulation, and eddy current. The failure location is highlighted in red. Scan locations and coordinate system are shown in Figures 15 and 16. The red dashed area corresponds to Area 2.

Adjacent Joint	Micro-CT	Simulation	EC 2D Measurement (Mean Vector) $V_x = \sin^2 \alpha, V_y = \cos^2 \alpha$
Area 1: 40 mm above the WL	$\begin{pmatrix} 0.51 & 0.01 & 0 \\ \text{sym.} & 0.49 & 0 \\ \text{sym.} & \text{sym.} & 0.01 \end{pmatrix}$	$\begin{pmatrix} 0.46 & 0.02 & 0 \\ \text{sym.} & 0.54 & 0 \\ \text{sym.} & \text{sym.} & 0 \end{pmatrix}$	$\begin{bmatrix} 0.60 & . \\ . & 0.40 \end{bmatrix}$
Area 2: ±20 mm around the WL	$\begin{pmatrix} 0.54 & 0.03 & 0 \\ \text{sym.} & 0.46 & 0 \\ \text{sym.} & \text{sym.} & 0.01 \end{pmatrix}$	$\begin{pmatrix} 0.51 & 0.01 & 0 \\ \text{sym.} & 0.49 & 0 \\ \text{sym.} & \text{sym.} & 0 \end{pmatrix}$	$\begin{bmatrix} 0.64 & . \\ . & 0.37 \end{bmatrix}$
Area 3: 40 mm below the WL	$\begin{pmatrix} 0.52 & 0.04 & 0 \\ \text{sym.} & 0.47 & 0 \\ \text{sym.} & \text{sym.} & 0.01 \end{pmatrix}$	$\begin{pmatrix} 0.47 & -0.03 & 0 \\ \text{sym.} & 0.53 & 0 \\ \text{sym.} & \text{sym.} & 0 \end{pmatrix}$	$\begin{bmatrix} 0.62 & . \\ . & 0.39 \end{bmatrix}$

The orientation state measured by EC are showing similar trend of higher A11 component at the weld-line region, however higher A11 values to the values measured by Micro-CT in all 3 scan areas. To resolve this issue, further targeted studies are required to calibrate the EC method by using unidirectional carbon fibre tows rotated at known angles. This slight error can be a systematic error in alignment of the robot head to the define x-axis coordinate system. The results match in terms of higher A11 values for the Flow when compared to the A11 values of the Butt sample in scan area 2.

The results shown in this work are an important step towards realising the capability of EC testing in detecting defects for quality assurance in C-SMC. An example of an EC uniformity map obtained from a 3D generic beam geometry (versus a partially filled manufactured part) is shown in Figure 17. The dark regions on the upper face indicate out-of-plane flow and subsequent alignment of the carbon fibre tows into an underlying (out-of-plane) internal rib structure. Unexpectedly, the EC mapping taken from the side walls of this component also shows the presence of WLDs/resin-rich areas and out-of-plane fibre alignments that are not predicted by simulation models. The pattern obtained from EC testing matches the flow pattern seen in the partially filled counterpart.

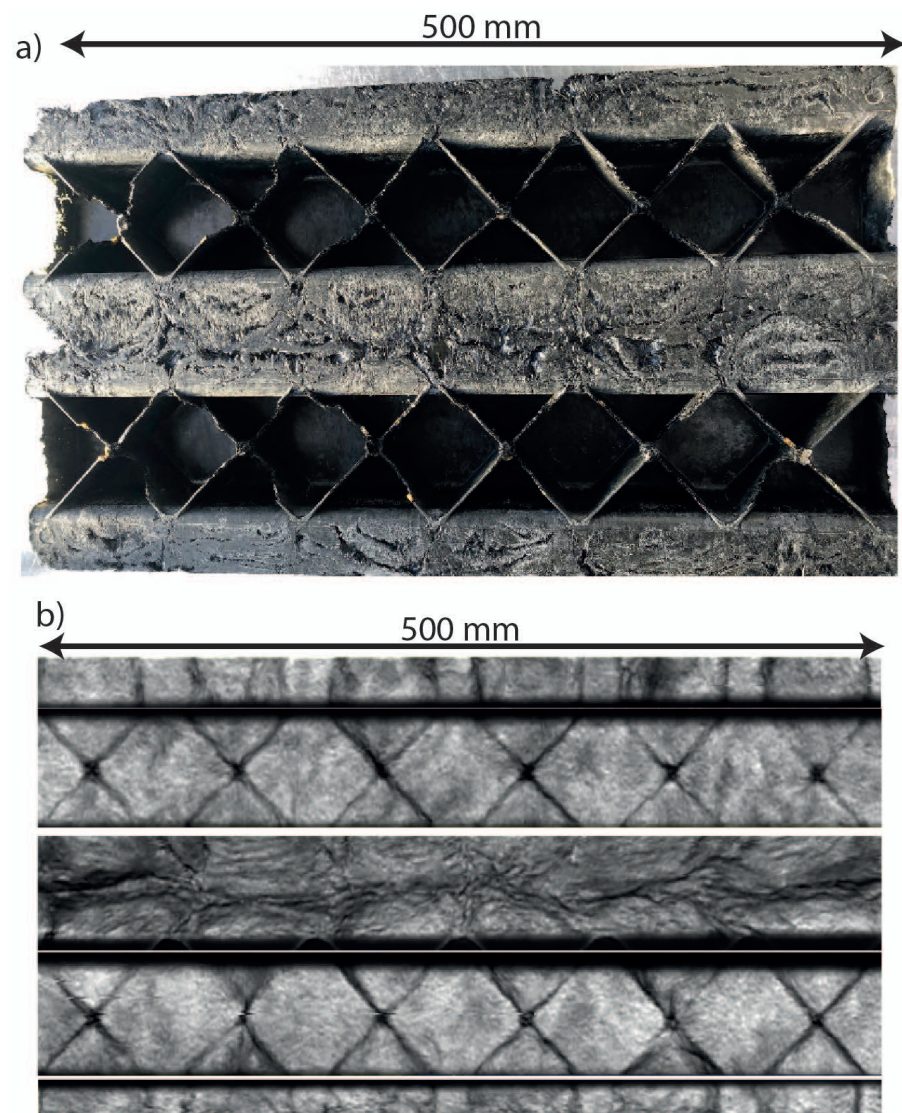


Figure 17. (a) A photo of a partially filled 3D structural CFRP part containing two characteristic “u-profile beams”. (b) EC real raw image obtained from the outer surfaces of a fully moulded twin characteristic “u-profile beam” 3D part with an underlying internal rib structure.

5. Conclusions

The effect of WLDs on the morphology and mechanical properties of the selected compression-moulded CF-SMC was shown using a combination of EC scanning, micro-CT, and mechanical testing with DIC strain mapping. In particular, it was shown that the introduction of a forced WLD can lead to a severe reduction in tensile strength (up to 80%). The opposing fronts were seen to behave as impermeable boundaries (analogous to the mould cavity walls), with no evidence of fibre intermingling across the fronts at the WLD. It was shown that this lack of fibre bridging across the WLD eliminates the contacts between adjacent carbon fibres, forming an electrical discontinuity that breaks the EC loops in the composite part. Carbon fibre tows were shown to be highly distorted at the weld-line, due to the material flow phenomena, with the highest distortions occurring near the edges of the mould. Defects such as voids and cracks were observed at the WLDs using multiple NDT methods, such as radiography, micro-CT, and EC, and compared to the process simulation results.

Furthermore, the technique can also successfully identify and characterise the critical variations in fibre content and alignment inherent in “forced defect free” carbon DFCs. Failure in DFCs occurs when a stress concentration (due to discontinuities in the micro-scale

and meso-scale structure) and material weakness coincide. Weakness in DFCs originates from discontinuities, such as in the fibre–matrix interface, and variation in the resin content in meso-scale structure. The discontinuities that lead to failure in DFCs significantly alter the EC complex impedance signal strength, making the EC technique highly sensitive to their presence and uniquely suited to their detection. Consequently, the total current density in the failed region is considered to decay for three reasons, (a) an overall reduction in the volume fraction of conductive fibre (resin-rich regions); (b) out-of-plane orientation of the fibres, thus reducing the in-plane current density; and (c) a continuous, linear electrical discontinuity, created due to the lack of fibre crossing. Using this phenomenon and performing EC scans at multiple sensor orientations, it was possible to elucidate both the local fibre-matrix content and local principal fibre angles at appropriate spatial resolutions for defect characterisation. Comparisons revealed that the principal fibre angle distributions determined from such four-directional EC scans correlated strongly with the distributions obtained by micro-CT for samples with WLDs.

As such, robot-guided EC scanning methods constitute a potential solution for detecting process-induced anisotropic microstructures non-destructively. Charge placement during the development of the moulding process for a given part can be optimised to eliminate or move defects away from critical locations, to reduce material waste and perform routine quality control during production.

Author Contributions: Conceptualization, N.F.-S. and N.R.; methodology N.F.-S., N.R., D.N., C.Q., P.S. and R.K.; software, D.J.A., P.S. and R.K.; validation, N.F.-S., D.J.A., C.Q. and D.N.; formal analysis, N.F.-S., N.R., D.J.A., C.Q., D.N. and P.S.; investigation, N.F.-S., N.R., P.S., R.K. and D.N.; resources, N.R., C.Q. and K.K.; data curation, N.F.-S., C.Q., D.N. and N.R.; writing—original draft preparation, N.F.-S.; writing—review and editing, N.F.-S., N.R., C.Q., D.N., D.J.A. and P.S.; visualization, N.F.-S., D.N. and C.Q.; funding acquisition, C.Q., K.K. and M.A.W. All authors have read and agreed to the published version of the manuscript.

Funding: This research was funded by APC10 TUCANA grant no. 113198, EPSRC Future Metrology Hub (grant number EP/P006930)1 and the EPSRC Future Composites Manufacturing Hub (grant number EP/P006701/1). D.J.A acknowledges support from the STFC via an Ernest Rutherford Fellowship (ST/R00384X/1).

Institutional Review Board Statement: Not applicable.

Informed Consent Statement: Not applicable.

Data Availability Statement: Not applicable.

Acknowledgments: The materials used in this work were moulded as part of an APC-funded CHAMAELEON at WMG by Richard Groves, and the authors would like to acknowledge the APC-funded TUCANA project consortium for their support in completing the study. We would like to thank Expert Tooling and Automation Ltd. for providing access to the Kuka robot and Adam Walton for robot integration.

Conflicts of Interest: The authors declare no conflict of interest.

References

1. Fereshteh-Saniee, N.; Reynolds, N.; Kelly, C.A.; Wilson, P.R.; Jenkins, M.J.; Kendall, K.N. Introducing cryomilling for reliable determination of resin content and degree of cure in structural carbon fibre reinforced thermoset composites. *Compos. Part A Appl. Sci. Manuf.* **2018**, *107*, 197–204. [[CrossRef](#)]
2. Gupta, J.; Reynolds, N.; Chiciudean, T.; Kendall, K. A comparative study between epoxy and vinyl ester CF-SMC for high volume automotive composite crash structures. *Compos. Struct.* **2020**, *244*, 112299. [[CrossRef](#)]
3. Centea, T.; Hubert, P. Measuring the impregnation of an out-of-autoclave prepreg by micro-CT. *Compos. Sci. Technol.* **2011**, *71*, 593–599. [[CrossRef](#)]
4. Qian, C.; Harper, L.; Turner, T.; Warrior, N. Notched behaviour of discontinuous carbon fibre composites: Comparison with quasi-isotropic non-crimp fabric. *Compos. Part A Appl. Sci. Manuf.* **2011**, *42*, 293–302. [[CrossRef](#)]
5. Selezneva, M.; Lessard, L. Characterization of mechanical properties of randomly oriented strand thermoplastic composites. *J. Compos. Mater.* **2016**, *50*, 2833–2851. [[CrossRef](#)]

6. Visweswaraiah, S.B.; Selezneva, M.; Lessard, L.; Hubert, P. Mechanical characterisation and modelling of randomly oriented strand architecture and their hybrids—A general review. *J. Reinf. Plast. Compos.* **2018**, *37*, 548–580. [CrossRef]
7. Feraboli, P.; Cleveland, T.; Ciccu, M.; Stickler, P.; DeOto, L. Defect and damage analysis of advanced discontinuous carbon/epoxy composite materials. *Compos. Part A Appl. Sci. Manuf.* **2010**, *41*, 888–901. [CrossRef]
8. Favaloro, A.J.; Tseng, H.-C.; Pipes, R.B. A new anisotropic viscous constitutive model for composites molding simulation. *Compos. Part A Appl. Sci. Manuf.* **2018**, *115*, 112–122. [CrossRef]
9. Chookaew, W.; Mingbunjurdsuk, J.; Jittham, P.; Ranong, N.N.; Patcharaphun, S. An Investigation of Weldline Strength in Injection Molded Rubber Parts. In *Energy Procedia, Proceedings of the 10th Eco-Energy and Materials Science and Engineering Symposium, Ubon-Ratchathani, Thailand, 5–8 December 2012*; Yupapin, P., PivsaArt, S., Ohgaki, H., Eds.; Elsevier: Amsterdam, The Netherlands, 2013; pp. 767–774.
10. Chrysostomou, A.; Hashemi, S. Mechanical properties of injection moulded styrene maleic anhydride (SMA) Part II Influence of short glass fibres and weldlines. *J. Mater. Sci.* **1998**, *33*, 4491–4501. [CrossRef]
11. Debondue, E.; Fournier, J.-E.; Lacrampe, M.-F.; Krawczak, P. Weld-line sensitivity of injected amorphous polymers. *J. Appl. Polym. Sci.* **2004**, *93*, 644–650. [CrossRef]
12. Fellahi, S.; Meddad, A.; Fisa, B.; Favis, B.D. Weldlines in injection-molded parts: A review. *Adv. Polym. Technol.* **1995**, *14*, 169–195. [CrossRef]
13. Hashemi, S. Thermal effects on weld and unweld tensile properties of injection moulded short glass fibre reinforced ABS composites. *Express Polym. Lett.* **2007**, *1*, 688–697. [CrossRef]
14. Baradi, M.B.; Cruz, C.; Riedel, T.; Régnier, G. Mechanical and microstructural characterization of flowing weld lines in injection-molded short fiber-reinforced PBT. *Polym. Test.* **2019**, *74*, 152–162. [CrossRef]
15. Quintana, M.C.; Frontini, P. Weld line strength factors in a reinforced injection molded part: Relationship with predicted fiber orientation. *J. Reinf. Plast. Compos.* **2019**, *39*, 219–230. [CrossRef]
16. Leblanc, D.; Landry, B.; Levy, A.; Hubert, P.; Roy, S.; Yousefpour, A.; Quinlan, E. Study of Processing Conditions on the Forming of Ribbed Features Using Randomly Oriented Strands Thermoplastic Composites. *J. Am. Helicopter Soc.* **2015**, *60*, 1–9. [CrossRef]
17. Martulli, L.; Creemers, T.; Schöberl, E.; Hale, N.; Kerschbaum, M.; Lomov, S.V.; Swolfs, Y. A thick-walled sheet moulding compound automotive component: Manufacturing and performance. *Compos. Part A Appl. Sci. Manuf.* **2020**, *128*, 105688. [CrossRef]
18. Martulli, L.; Kerschbaum, M.; Lomov, S.V.; Swolfs, Y. Weld lines in tow-based sheet moulding compounds tensile properties: Morphological detrimental factors. *Compos. Part A Appl. Sci. Manuf.* **2020**, *139*, 106109. [CrossRef]
19. Teuwsen, J.; Hohn, S.K.; Osswald, T.A. Direct Fiber Simulation of a Compression Molded Ribbed Structure Made of a Sheet Molding Compound with Randomly Oriented Carbon/Epoxy Prepreg Strands—A Comparison of Predicted Fiber Orientations with Computed Tomography Analyses. *J. Compos. Sci.* **2020**, *4*, 164. [CrossRef]
20. Auld, B.A.; Moulder, J.C. Review of Advances in Quantitative Eddy Current Nondestructive Evaluation. *J. Nondestruct. Eval.* **1999**, *18*, 3–36. [CrossRef]
21. Bardl, G.; Nocke, A.; Hübner, M.; Gereke, T.; Pooch, M.; Schulze, M.; Heuer, H.; Schiller, M.; Kupke, R.; Klein, M.; et al. Analysis of the 3D draping behavior of carbon fiber non-crimp fabrics with eddy current technique. *Compos. Part B Eng.* **2018**, *132*, 49–60. [CrossRef]
22. Berger, D.; Lanza, G. Development and Application of Eddy Current Sensor Arrays for Process Integrated Inspection of Carbon Fibre Preforms. *Sensors* **2017**, *18*, 4. [CrossRef] [PubMed]
23. Cheng, J.; Ji, H.; Qiu, J.; Takagi, T.; Uchimoto, T.; Hu, N. Role of interlaminar interface on bulk conductivity and electrical anisotropy of CFRP laminates measured by eddy current method. *NDT E Int.* **2014**, *68*, 1–12. [CrossRef]
24. Heuer, H.; Schulze, M.; Pooch, M.; Gäbler, S.; Nocke, A.; Bardl, G.; Cherif, C.; Klein, M.; Kupke, R.; Vetter, R.; et al. Review on quality assurance along the CFRP value chain—Non-destructive testing of fabrics, preforms and CFRP by HF radio wave techniques. *Compos. Part B Eng.* **2015**, *77*, 494–501. [CrossRef]
25. Hughes, R.R.; Drinkwater, B.W.; Smith, R.A. Characterisation of carbon fibre-reinforced polymer composites through radon-transform analysis of complex eddy-current data. *Compos. Part B Eng.* **2018**, *148*, 252–259. [CrossRef]
26. Schulze, M.H.; Heuer, H.; Küttner, M.; Meyendorf, N. High-resolution eddy current sensor system for quality assessment of carbon fiber materials. *Microsyst. Technol.* **2010**, *16*, 791–797. [CrossRef]
27. Bardl, G.; Nocke, A.; Cherif, C.; Pooch, M.; Schulze, M.; Heuer, H.; Schiller, M.; Kupke, R.; Klein, M. Automated detection of yarn orientation in 3D-draped carbon fiber fabrics and preforms from eddy current data. *Compos. Part B Eng.* **2016**, *96*, 312–324. [CrossRef]
28. Khan, A.M.; Bardl, G.; Nocke, A.; Cherif, C. Quality analysis of 2D and 3D-draped carbon preforms by eddy current scanning. *Compos. Part B Eng.* **2019**, *176*, 107110. [CrossRef]
29. Suragus GmbH. Available online: <https://www.suragus.com/en/products/carbon-fiber-testing/portable-devices/portable-handheld-for-carbon-fiber-testing/> (accessed on 15 October 2019).
30. Feraboli, P.; Peitso, E.; Cleveland, T.; Stickler, P.B. Modulus Measurement for Prepreg-based Discontinuous Carbon Fiber/Epoxy Systems. *J. Compos. Mater.* **2009**, *43*, 1947–1965. [CrossRef]

31. Evans, A.; Qian, C.; Turner, T.; Harper, L.; Warrior, N. Flow characteristics of carbon fibre moulding compounds. *Compos. Part A Appl. Sci. Manuf.* **2016**, *90*, 1–12. [[CrossRef](#)]
32. Feraboli, P.; Peitso, E.; Cleveland, T.; Stickler, P.B.; Halpin, J.C. Notched behavior of prepreg-based discontinuous carbon fiber/epoxy systems. *Compos. Part A Appl. Sci. Manuf.* **2009**, *40*, 289–299. [[CrossRef](#)]